Journal of Physics:
Conference Series

PAPER • OPEN ACCESS

Parametric optimization of pore characteristics for enhanced acoustic attenuation in coated underwater shells

To cite this article: Xiangxi Bu 2026 *J. Phys.: Conf. Ser.* **3170** 012003

Parametric optimization of pore characteristics for enhanced acoustic attenuation in coated underwater shells

Xiangxi Bu*

Makarov College of Marine Engineering, Jiangsu Ocean University, Lianyungang, 222005, Jiangsu, China

*Corresponding author's e-mail: 2022124448@jou.edu.cn

Abstract. By modeling interactions between vacuum and porous materials through multiphysics coupling mechanisms at fluid-solid interfaces in a two-dimensional (2D) finite element (FE) acoustic-structural framework, this paper employs vibroacoustic coupling methodologies to systematically analyse parametric underwater vehicle acoustic coatings performance, quantifying the effects of pore geometries, particularly shapes, scales and spatial configurations on radiated sound pressure level (SPL). Numerical results derived from Green's function, etc., demonstrate coatings provide up to $50\ dB$ attenuation within $100{\sim}500$ Hz, circular apertures consistently outperform square and triangular ones by $50\ dB$ above $100\ Hz$, whereas larger pore radii and multi-row designs induce progressive attenuation over mid- and low- frequency spectrum ($0{\sim}1500\ Hz$).

1. Introduction

The development of anechoic coatings traces back to the 1930s, pioneered by German acoustician Erwin Meyer [1], who seminally conceptualized and experimentally validated viscous fluids or polyisobutylene rubbers as submarine anechoic surface tiles, formulating a systematic measurement framework. Resonant absorption mechanisms emerged from analyses of bubble dynamics and suspended particle-fluid interactions in fluids, later evolving to encompass engineered cavities and filler-reinforced optimized viscoelastic composites. Early experimental studies have established that thickness-mode resonance in homogeneous acoustic materials, synergistically coupled with bubble resonance in viscoelastic media and cavity-induced resonance in elastomeric substrates, dramatically enhance broadband acoustic absorption and transmission loss (TL) in such coatings. As a cornerstone of hydroacoustics, Alberich-type periodic lattice coatings composed of identical unit cells, have demonstrated superior absorption coefficients and broadband TL, thereby enabling acoustic wave manipulation. Building upon the established paradigm of periodic cavity configurations, Ivansson [2] developed innovative Alberich-type dual-periodic acoustic coatings incorporating carefully engineered cavity arrays with tunable resonance coupling, achieving enhanced broadband impedance matching and superior frequency-selective sound attenuation. Sharma [3] engineered a polydimethylsiloxane (PDMS)-matrix cylindrical perforated cavity configuration, quantified its broadband absorption performance via a novel mathematical framework, and numerically mapped resonance-driven displacement patterns through finite element analysis (FEA), with absorption peak formation mechanisms rigorously analyzed through the Fabry-Pérot resonant conditions. Valentin Leroy [4] developed a PDMS-based ultrathin 230 μm acoustic metastructure incorporating a microperforated rectangular cavity array, where cavity-substrate coupling resonance synergistically interacts with intrinsic viscoelastic damping of the polymeric matrix to govern subwavelength absorption performance. Diverging from conventional viscous-thermal Alberich absorbers, Hunki Lee [5] devised an innovative acoustic metasurface architecture via advanced electron microscopy-assisted nanofabrication, operating on a divergent wave-manipulation paradigm distinct from classical Alberich-type absorption mechanisms. Hasheminejad [6] developed an impedance-graded metamaterial with compositionally tailored zirconia-aluminium gradients, enabling spectral tuning of absorption maxima through gradient index modulation for broadband absorption enhancement. Méresse [7] characterized wave propagation dynamics in multilayer phononic metastructures with periodic soft-hard interfaces, revealing impedance-mismatch-induced bandgap formation mechanisms. Hou [8] systematically conducted an investigation into sound transmission mechanisms in flexible micro-perforated panels (FMPP), with particularly emphasis on broadband attenuation performance, extended the analytical framework to encompass a novel class of underwater viscoelastic metamaterials, elucidating void-induced effects by dominating the sophisticated hybrid numerical-experimental methodologies.

2. Numerical modeling and experimental validation via finite element method (FEM)

2.1. Numerical framework and model parametrization

The computational model based on a validated experimental framework of a 2D cylindrical steel shell is coated with porous acoustic metamaterial layers optimized for underwater radiated-noise simulations [9], employing finite element formulations with coupled acoustic–structure interactions to ensure prediction fidelity through cross-validation with empirical benchmarks, rigorously enhancing reliability and credibility of numerical predictions and integrates vibroacoustic response, as shown in Figure 1 [10].

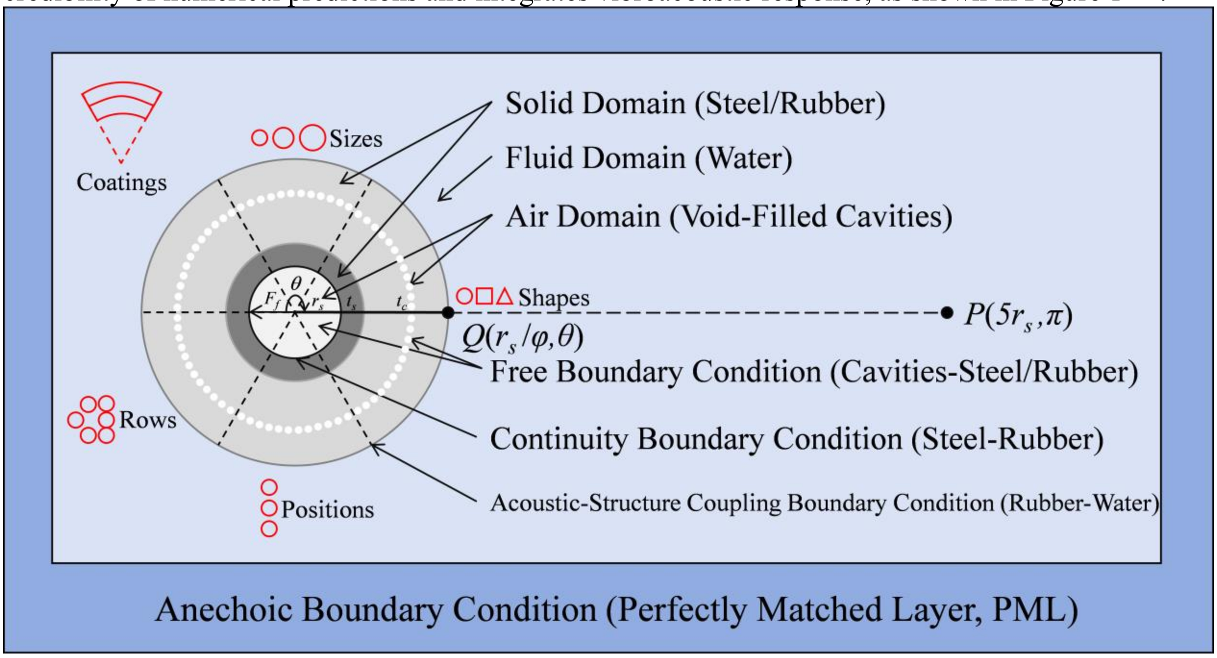

Figure 1. Schematic diagram of conceptually cylindrical model with multiple domains and specific conditions.

Table 1. Material properties for viscoelastic shell, coating, liquid, and gas phases in the 2D vibroacoustic model.

Material	Density	Poisson's ratio	Elastic modulus	Shear modulus	Loss factor	Damping ratio
Steel	$7800\ \mathrm{kg/m^3}$	0.300	$175 - 3.5i$ GPa	$80.77 - 1.6i$ GPa	0.02	0.010
Rubber	$1000\ \mathrm{kg/m^3}$	0.499	$1 - 0.01i$ GPa	$0.0006 - 0.00018i$ GPa	0.01	0.005
Water	$1000\ \mathrm{kg/m^3}$	Speed of sound in water is 1500 m/s				
Air	$1.29\ \mathrm{kg/m^3}$	Speed of sound in air is 340m/s				

The cylindrical shell is numerically modeled in COMSOL Multiphysics® with a viscoelastic rubber coating of thickness $t_c = 0.1\ m$, uniformly clad onto a steel substrate characterized by radius $r_s = 1\ m$ and wall thickness $t_s = 0.01\ m$, under horizontal point force excitation of amplitude $F_f = 1N$, while circumferential rubber layer features $N = 60$ azimuthally periodic air-filled pores distributed along central circumference, each with a nominal diameter $d = 0.05\ m$. Material parameters for structural materials (steel/rubber), aqueous medium (water) and gaseous medium (air) are comprehensively tabulated in Table 1 [11], with both steel and rubber characterized by complex-valued viscoelastic moduli, where real component governs elastic stiffness and imaginary component quantifies intrinsic damping [12].

2.2. Mesh convergence and numerical verification

The vibroacoustic domains are discretized by using FEM, with material-specific viscoelastic constitutive relationships assigned to individual elements. Computational fidelity and numerical accuracy in resolving the minimum dominant frequency (f_{min}) are ensured by enforcing rigorous mesh refinement criteria, mandating at least more than six nodes per wavelength ($N_\lambda \geq 6$) within the sufficiently discretized domain to achieve spectral convergence criteria. Figure 2 confirms the spatial accuracy and convergence behavior, verifying that the discretization step satisfies the criterion ($\Delta r < \lambda/6$), thereby guaranteeing both the spectral accuracy and numerical reliability. The numerical framework is further validated via comprehensive multiphysics simulations performed in COMSOL Multiphysics®, with detailed results including total sound pressure, SPL, stress distributions, and force responses shown in Figure 3.

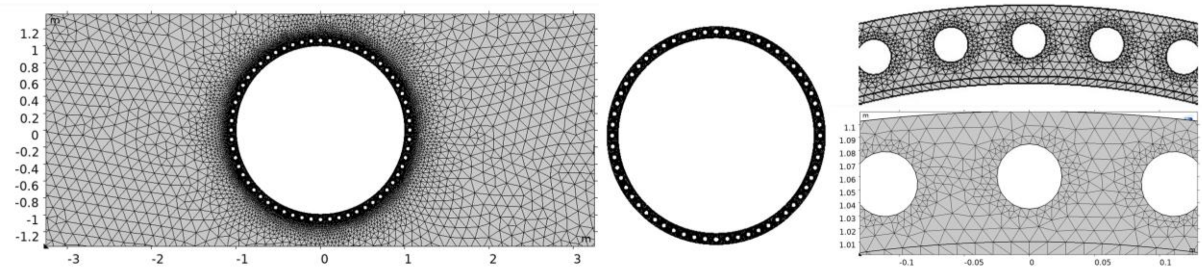

Figure 2. Discretized hybrid mesh independence convergence verification in a detailed vibroacoustic FE model.

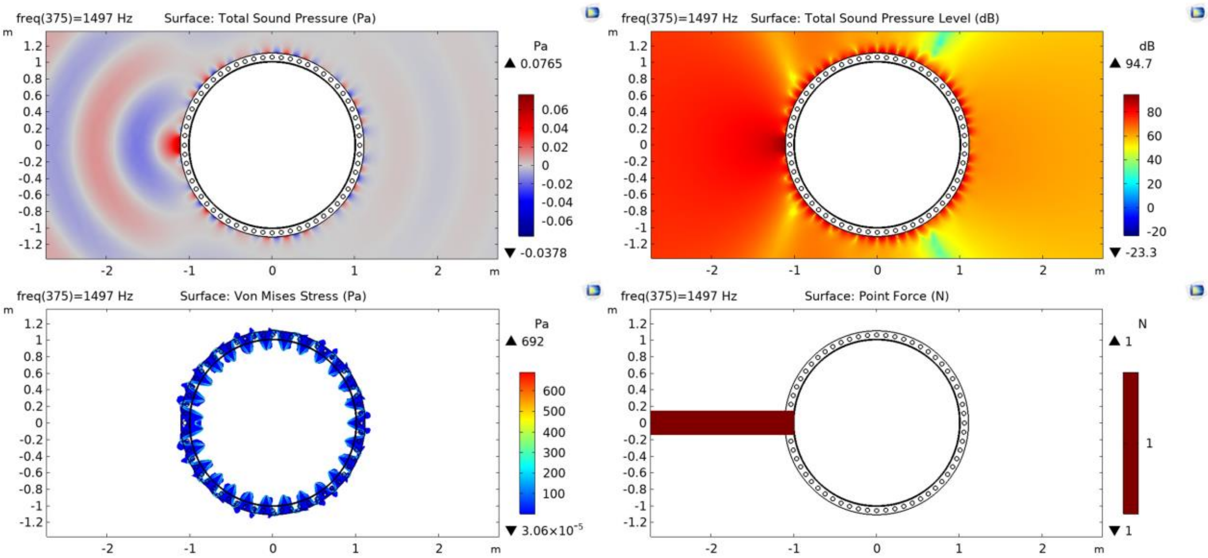

Figure 3. Numerical simulation results for total sound pressure, total SPL, von mises stress, and point force.

3. Formula derivation and theoretical calculation

3.1. Acoustic continuity conditions via the Bessel–Neumann approach at perforated layer interfaces

The continuous transmission conditions governing acoustic wave behavior at the interfaces between cylindrical cavities and perforated cover layers are mathematically described by the coupling matrix system presented below, captures essential acoustic–structural interactions and fundamentally influences wave propagation mechanisms in complex media, as characterized by Bessel–Neumann approach.

$$\left\{\begin{bmatrix} J_0(k_1 r_s) & N_0(k_1 r_s) \\ J_1(k_1 r_s) & N_1(k_1 r_s) \\ J_0(k_1 r_s/\varphi) & N_0(k_1 r_s/\varphi) \\ J_1(k_1 r_s/\varphi) & N_1(k_1 r_s/\varphi) \end{bmatrix}\begin{pmatrix} C_1 \\ C_2 \end{pmatrix}\right\}^T \begin{pmatrix} 1-\dfrac{k_s^2}{2k'^2} \\ \dfrac{k_1}{k'^2 r_s} \\ 0 \\ \dfrac{k_1}{k'} \end{pmatrix} = \left\{\begin{bmatrix} J_0(k_2 r_s) & N_0(k_2 r_s) \\ J_1(k_2 r_s) & N_1(k_2 r_s) \\ J_0(k_2 r_s/\varphi) & N_0(k_2 r_s/\varphi) \\ J_1(k_2 r_s/\varphi) & N_1(k_2 r_s/\varphi) \end{bmatrix}\begin{pmatrix} C_3 \\ C_4 \end{pmatrix}\right\}^T \begin{pmatrix} -1 \\ \dfrac{1}{k_2 r_s} \\ 0 \\ \dfrac{k'}{k_2} \end{pmatrix} \quad (1)$$

Here, J_τ and N_τ denote the Bessel and Neumann functions of order $\tau, \tau = 0,1,\cdots$, with approximations $J_0(kr) \approx [1-(kr)^2/4+(kr)^4]/192$, $J_1(kr) \approx kr[1-(kr)^2/8+(kr)^4/192]/2$. The acoustically equivalent complex wave numbers are $k = \omega/\mathrm{c}, k' = \omega/c'$, with additional wave numbers $k_1 = (k_L^2 - k^2)^{1/2}, k_2 = (k_s^2 - k^2)^{1/2}$, where $k_L = \omega[\rho/(\lambda+2\mu)]^{1/2}$, $k_s = \omega(\rho/\mu)^{1/2}$ are the longitudinal and transverse acoustic wave numbers, with the Lamé constants λ, μ. The coefficients C_1, C_2, C_3, C_4 are determined by specific boundary conditions, while effective impedance, density, porosity, and sound speed of perforated layers are $Z_i = \rho_i c_i, \rho_i = \rho_e(1-\varphi^2) + \rho_A\varphi^2, \varphi = r_s/(r_s + t_s + t_c), c_i = \omega_i / k$.

3.2. Resonance frequency and viscous boundary layers formulation in rigid-backed cavities

The resonance frequencies of a viscoelastic cylindrical cavity with rigid backing are $f_1 = c_e/(4t)$ and $f_2 = 3c_e/(4t)$, where the equivalent sound speed $c_e = \{\lambda\mu(1+3\alpha^2)/[\rho_e(\mu+\lambda\alpha^2)]\}^{1/2}$, while the first absorption peak frequency f_{max} specifically occurs between f_1 and f_2 at the midpoint $f_{max} = (f_1+f_2)/2 = c_e/(2t)$. The viscous boundary layer thickness is $\delta = 220[\mu m] \times (100/f_{max})^{1/2}$. A fundamental method to solving the Laplace's equation, i.e., the Green's function $G(P,Q)$, satisfies $\nabla^2\phi G(P,Q) = -\delta(P,Q)$, where the 2D Laplace operator ∇^2 in polar coordinates (r,θ) is $\nabla^2\phi = \partial\phi(r\,\partial\phi/\partial r)/(r\partial r) + (\partial^2\phi/\partial\theta^2)/r^2 = 0$, and the Dirac delta function δ is $\delta(P,Q) = 0$ for $r_P = r_Q$, $\iint_\Omega \delta(P,Q)\, d\Omega\,(Q) = 1$. The 2D free-field Green's function takes symmetrical form from $G(P,Q) = G(Q,P) = -ln\, r(P,Q)/(2\pi)$, where $r(P,Q) = r = |P-Q|$ is Euclidean distance between points P and Q. The Helmholtz-Kirchhoff Integral Theorem (HKIT) in boundary integral equation (BIE) yields

$$c(P)p(P) = \int_S [p(Q)\,\partial G(P,Q)/\partial \mathrm{n} + \mathrm{j}\rho_0\omega\phi_n(Q)G(P,Q)]\mathrm{d}S(Q) \quad (2)$$

where $c(P) = \theta/(4\pi)$ is the geometric coefficient at point P on the vibrating source surface S, with the solid angle $\theta = \pi$, satisfying the relationship between acoustic pressure $p(Q)$ and normal derivative $\partial p(Q)/\partial n$ (or normal velocity $\phi_n(Q)$). By incorporating the continuity of normal velocity $\phi_n(Q) = j[\partial p(Q)/\partial n]/(\rho_0\omega)$ at interfaces. At infinity, the external acoustic far-field strictly obeys the Sommerfeld radiation condition $\lim_{r\to\infty}[r(\partial p_\infty/\partial r + jkp_\infty)] = 0$, with r confined to $r_s \ll 4r_s \le r \le 6r_s$.

3.3. Green's function fundamental solutions for acoustic wave equations in cylindrical coordinates

The circular frequency ω, displacement function $u(r,\theta,)$ and tension T obey the governing equation $\partial[r\partial u(r,\theta)/\partial \mathrm{r}]/(r\partial r) + [\partial^2 u(r,\theta)/\partial\theta^2]/r^2 + \omega^2\rho(r)u(r,\theta)/\mathrm{T} = 0, r_s < r < r_s/\varphi, 0 \leqslant \theta \leqslant 2\pi$. Applying the separation of variables $u(r,\theta) = R(r)\Phi(\theta)$ leads to the radial and angular equation $Td[rdR(r)/\mathrm{d}r]/(rdr) + [\omega^2\rho(r) - Tm^2/r^2]R(r) = 0, \Phi''(\theta) + m^2\Phi(\theta) = 0$, while boundary conditions $\begin{cases} T\partial u(r,\theta)/\partial \mathrm{r}|_{r=r_s} - ku(r_s,\theta) = 0 \\ T\partial u(r,\theta)/\partial \mathrm{r}|_{r=r_s/\varphi} + hu(r_s/\varphi,\theta) = 0 \end{cases} \Rightarrow \begin{cases} TR'(r_s) - kR(r_s) = 0 \\ TR'(r_s/\varphi) + hR(r_s/\varphi) = 0 \end{cases}$. The radial Green's function $G(r,Q)$ satisfies the homogeneous equation $-T\{d[rdG(r,Q)/\mathrm{d}r]/\mathrm{d}r + m^2G(r,Q)/\mathrm{r}\} = 0, \begin{cases} r_s \leqslant r \\ Q \leqslant r_s/\varphi \end{cases}$, subject to boundary conditions $\begin{cases} TG'(r_s,Q) - kG(r_s,Q) = 0 \\ TG'(r_s/\varphi,Q) + hG(r_s/\varphi,Q) = 0 \end{cases}$, and connection conditions at $r = Q$ is $-Tr[(dG/\mathrm{d}r)_{r=s^+} - (dG/\mathrm{d}r)_{r=s^-}] = 1$, with $G(r,Q)$ continuous. In the limiting case of clamped boundaries, and the coefficients $k, h \to +\infty$, the Green's function $G(r,Q)$simplifies to

$$G(r,Q) = \begin{cases} [ln(r/r_s)][ln(Q\varphi/r_s)]/(Tln\varphi), r_s \leqslant r < Q \\ [ln(Q/r_s)][ln(r\varphi/r_s)]/(Tln\varphi), Q \leqslant r \leqslant r_s/\varphi \end{cases} \quad (3)$$

3.4. Multilayer acoustic propagation and holes impedances through transfer matrix method (TMM)
The TMM is used to model acoustic wave propagation in multilayered structures, wherein the relationship between the input initial pressure p_0 and normal vibration velocity ϕ_0, the corresponding output quantities p_{i+1} and ϕ_{i+1} is $[p_0 \quad \phi_0] = T_{Total}[p_{i+1} \quad \phi_{i+1}]$. So the total transfer matrix (TM) T_{Total} is

$$T_{Total} = \prod_{i=1}^{n} T_i = T_{Air\ layer} \cdot T_{Steel\ layer} \cdot T_{Rubber\ uniform\ layer\ 1} \cdot T_{Rubber\ perforated\ layer} \cdot T_{Rubber\ uniform\ layer\ 2} \cdot T_{Water\ layer} = T_A \cdot T_S \cdot T_{RU1} \cdot T_{RP} \cdot T_{RU2} \cdot T_W = \begin{bmatrix} T_{11} & T_{12} \\ T_{21} & T_{22} \end{bmatrix} s.t. n = 6 \quad (4)$$

For a generic layer i, TM is $T_i = \begin{bmatrix} cos(k_i t_i) & jZ_i S\, sin(k_i t_i) \\ jsin(k_i t_i)/(Z_i S) & cos(k_i t_i) \end{bmatrix}, Z_i = p_i/\phi_i = \rho_i c_i$, i.e., $\begin{cases} Z_0 = p_0/\phi_0 \\ Z_\infty = p_{i+1}/\phi_{i+1} \end{cases}$. Note $\begin{cases} T_S = T_{MPP} \\ T_{RU1} = T_{RU2} = T_{RU} \end{cases}, S = \pi[(1-\varphi^2)(r_s/\varphi)^2 - N(d/2)^2]$. $T_{11}, T_{12}, T_{21}, T_{22}$ are elements of TM modeling acoustic wave propagation. For a micro-perforated panel (MPP), TM is $T_{MPP} = \begin{bmatrix} 1 & Z_{MPP} \\ 0 & 1 \end{bmatrix}$, with the acoustic impedance $Z_{MPP} = 32\eta t\{[(1 + k^2/32)^{1/2} + \sqrt{2}kd/(8t)] + \mathrm{j}\omega t[1 + (3^2 + k^2/2)^{-1/2} + 17d/(20t)]\}/(\rho d^2), k = \mathrm{d}(\pi f \rho/2\eta)^{1/2}$, where d, η, t, f, ω are the drilling diameter, air dynamic viscosity, MPP thickness, frequency, and angular frequency. Circular short tube holes acoustic impedance is $Z_C = 32\eta t\{(1 + k_c^2/32)^{1/2} + j\omega\rho_0 t[1 + (3^2 + k_c^2/2)^{-1/2}]\}/d^2, k_c = d(\omega/\mu)^{1/2}/2$, where μ is kinematic viscosity. Equilateral triangular holes acoustic impedance $Z_T = \omega\rho_0 t\left\{315^2[k_A(21 + 4k_A^2/21)]^{-2} + \left[(\sqrt{2}-1)k_A k_W\right]^2 k_V^{-2}\right\}^{1/2} + i\omega\rho_0 t\{30^2[k_A(21 + 4k_A/21)]^{-2} + [k_A(k_A - k_W)]^2 k_V^{-2}\}^{1/2}, k_V = (k_A - k_W)^2 + (5/2 - k_W)^2, k_A = k_t^2, k_W = 3k_t/\sqrt{2}, k_t = b(3\omega\rho_0/\eta)^{1/2}/4$, where b is equilateral triangle side length. Square holes acoustic impedance is $Z_{Sq} = a\rho_0 r_s(\pi^2/2k_{sq})^2 \sum_{n=0}^{\infty} [m^2(2\pi^2 m + k_{sq}\sqrt{j})], m = (n+1/2)^2, \sqrt{j} = \mathrm{e}^{j\pi/4} = (1+j)/\sqrt{2}$. For the steel layer, TM is $T_S = \begin{bmatrix} cos(k_s t_s) & jZ_s S\, sin(k_s t_s) \\ jsin(k_s t_s)/(Z_s S) & cos(k_s t_s) \end{bmatrix}, Z_s = \rho_s c_s$. For a uniform rubber layer, TM is $T_{RU} = \begin{bmatrix} cos(\overline{k_{RU}} t_{RU}) & jZ_R S\, sin(\overline{k_{RU}} t_{RU}) \\ jsin(\overline{k_{RU}} t_{RU})/(Z_R S) & cos(\overline{k_{RU}} t_{RU}) \end{bmatrix}, \begin{cases} Z_R = \rho_R c_R \\ t_{RU} = t_c - d \end{cases}$. The effective cross-sectional area function is $S(r) = \pi r^2$, and curvature term is $\mu^2 = \{[S(r)]^{1/2}\}''/[S(r)]^{1/2}$. Under the assumption that $\bar{k}^2 \gg \mu^2$, and $\bar{K}^2 = \bar{k}^2 - \mu^2 > 0$, for the perforated rubber layer, TM is $T_{RP} = \begin{bmatrix} cos\,\gamma + \frac{A}{2\bar{K}r_1} sin\,\gamma & \frac{j\bar{Z}_R S}{\bar{k}}\left\{\frac{B-A}{2S} cos\,\gamma + \left[\bar{K} + \frac{AB}{\bar{K}(2S)^2}\right] sin\,\gamma\right\} \\ \frac{j\bar{k}}{\bar{K}\bar{Z}_R S} sin\,\gamma & cos\,\gamma - \frac{B}{2\gamma} sin\,\gamma \end{bmatrix}, \begin{cases} A = \left(\frac{\mathrm{d}S}{\mathrm{d}r}\right)_{r=r_1} \\ B = \left(\frac{\mathrm{d}S}{\mathrm{d}r}\right)_{r=r_2} \end{cases}, \begin{cases} \gamma = \bar{K}r_2 \\ r_1 = r_s/\varphi \\ r_2 = r_1 - t_c/2 \\ \bar{Z}_R = \rho_R \bar{c}_R \end{cases}$. For the free-field water layer, TM is $T_W = \begin{bmatrix} cos(k_W t_W) & jZ_W S\, sin(k_W t_W) \\ jsin(k_W t_W)/(Z_W S) & cos(k_W t_W) \end{bmatrix}, \begin{cases} Z_W = \rho_W c_W \\ t_W = 4r_s - t_c - t_s \end{cases}$.

3.5. Integrated acoustic impedance formulations for cavities and porous materials media synthesis
The total acoustic impedance equals the sum of predominant contributions from individual components

$$Z_{Total} = \sum_{i=1}^{m} Z_i = Z_C + Z_M + Z_P + Z_D + Z_W\ s.t. m = 5, Z_{Av} = Z_{Total}/m \quad (5)$$

where cavity impedance is $Z_C = \rho c^2/(j\omega V), V = S_c t, S_c = \pi(r_s/\varphi)^2 - S = \pi[r_s^2 + N(d/2)^2]$. MPP relative impedance is $Z_M = (Z_{resi} + Z_{reac})/(\varphi Z_0)$, where Z_{resi} and Z_{reac} are calibrated resistance and reactance. Porous material acoustic impedance is widely predicted by Johnson-Champoux-Allard (JCA) model, and the Zwicker-Kosten method $Z_P = -\mathrm{j}[\rho(\omega)K(\omega)]^{1/2} cot\{\omega[\rho(\omega)K(\omega)]^{1/2} t\}$, with equivalent dynamic density $\rho(\omega) = \rho_0\alpha_\infty\left[1 - j\sigma\varphi\sqrt{1 + j4\rho_0\omega\eta\alpha_\infty^2/(\sigma^2\varphi^2\Lambda^2)}/(\omega\rho_0\alpha_\infty)\right]\varphi^{-1}$ and bulk modulus $K(\omega) = \gamma p_0 \left\{\gamma - (\gamma - 1)\left[1 - j8\eta/(\omega\rho_0 Pr\Lambda'^2)\sqrt{1 + j\omega\rho_0 Pr\Lambda'^2/(16\eta)}\right]^{-1}\right\}^{-1} \varphi^{-1}$, where $\sigma, \alpha_\infty, p_0, \eta, \gamma, Pr, \Lambda = 2[2\alpha_\infty\eta/(\sigma\varphi)]^{1/2}/\mathrm{c}, \Lambda' = 2[2\alpha_\infty\eta/(\sigma\varphi)]^{1/2}/c'$ are the static flow resistivity, tortuosity, ambient pressure, dynamic viscosity, specific heat ratio, Prandtl number, viscous and thermal characteristic lengths, respectively. Cavities impedance is $Z_D = -\mathrm{j}\cot[\omega(d + r_s)/c_0]$. Water impedance is given. The average impedance is $Z_{Av} = \sum_{\mathrm{i}=0}^{m} p_i \,/\, \sum_{\mathrm{i}=0}^{m} \varphi_i$, where $p_i, \varphi_i = \left[\left(\int_S |\varphi_i^2|\,\mathrm{d}S\right)/S\right]^{1/2}$ are the sound pressure and radial root mean square (RMS) vibration velocity value at point P, collectively characterizing the vibroacoustic response by the corresponding level in decibels (dB) is $\Delta L_v = 20\,lg(\varphi_m/\varphi_0)$, where the initial reference velocity is conventionally expressed as $\varphi_0 = 1 \times 10^{-9} m/s$.

3.6. Various novel acoustic absorption coefficient, capacity, TL and radiated SPL formulations

The absorption coefficient quantifies fractions of incident sound power absorbed, $\alpha = 1 - |r|^2 - |t|^2$, where $r = \frac{[t(T_{11}+T_{12}/Z_t - Z_iT_{21} - Z_iT_{22}/Z_t)\sqrt{Z_t/Z_i}]}{2}, t = \frac{2}{(T_{11}+T_{12}/Z_t+Z_iT_{21}+Z_iT_{22}/Z_t)}$ are reflection and transmission coefficient, and Z_i, Z_t are acoustic incident and transmitted media impedance, respectively. Instead, the absorption coefficient derived from surface impedance $Z_S = T_{11}/T_{21}$ and air $Z_A = \rho_A c_A$ is $\alpha = 4Re(Z_S/Z_A)/\{[1 + Re(Z_S/Z_A)]^2 + [Im(Z_S/Z_A)]^2\}$, where real part Re and imaginary part Im are associated with structure factor and flow resistivity. Related acoustic metrics in terms of SPL include differences $\Delta L_a = 10\,lg[(\alpha_2/\alpha_1)(1 - \alpha_1)/(1 - \alpha_2)]$, where $\alpha_{max} = \alpha_2 \geq \alpha_1 = \alpha_{min}$, damping-induced reduction $\Delta L_d = 10\,lg[(\eta_2/\eta_1)(1 - \eta_1)/(1 - \eta_2)]$, where $\eta_{max} = \eta_2 \geq \eta_1 = \eta_{min}$, and reflected volume ΔL_r is the same. In addition, TL is $TL = -20\mathrm{lg}|t|$, insulation value is $\Delta L_t = TL/2$. The effective sound pressure value p_e relative to reference value $p_{ref} = 1 \times 10^{-6} Pa$ takes the form

$$SPL_{Radiated\ in\ Valid\ Value} = 20lg|\,p_e/p_{ref}\,| = |\Delta L_v| - (|\Delta L_a| + |\Delta L_d| + |\Delta L_r| + |\Delta L_t|) \quad (6)$$

4. Parametric optimization [13] of vibroacoustic radiation control from underwater shells with metasurface coatings via bandgap superposition engineering [14], analyzed and evaluated by SPL

The radiated SPL is evaluated at the far-field point $P(r, \theta) = (5r_s, \pi)$ through COMSOL Multiphysics® vibroacoustic simulations in parametric analysis of coating configuration effects on acoustic radiation.

4.1. Comparison of radiated SPL by uncoated and coated configurations in acoustic metasurfaces

Figure 4 compares radiated SPL between uncoated and uniformly coated cylindrical shells. The coated shell exhibits frequency-dependent amplification in acoustic radiation, as evidenced in Figure 5, which is attributed to coupled vibroacoustic and hydrodynamic interactions between solids and liquids [15].

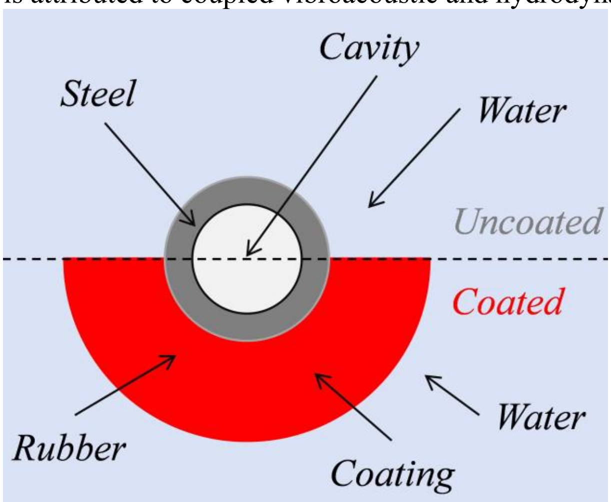

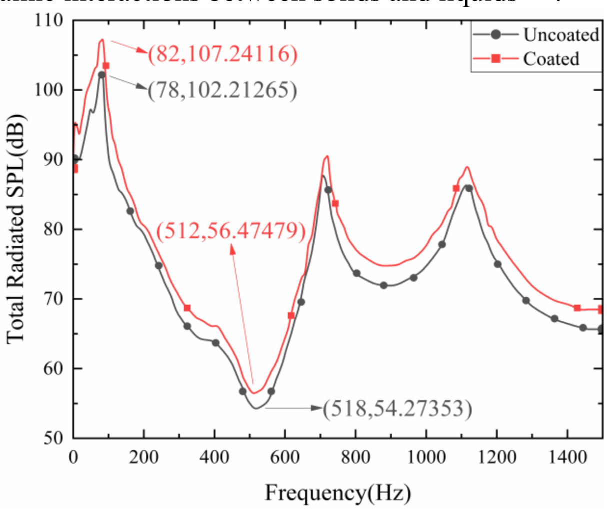

Figure 4. Acoustic model without or with the coating. **Figure 5.** Radiated SPL comparison: Uncoated or Coated.

4.2. Comparison of radiated SPL by various pore sizes configurations in acoustic metasurfaces
Figure 6 presents the frequency-dependent acoustic pressure radiation from an acoustically coated shell with circular pores of radii $0.020\ m, 0.025\ m, 0.030\ m$, obtained through vibroacoustic simulations. Below $400\ Hz$, larger aperture radii correspond to reduced radiated SPL over the frequency band, exerting negligible effects of pore sizes on acoustic radiation characteristics as entirely shown in Figure 7.

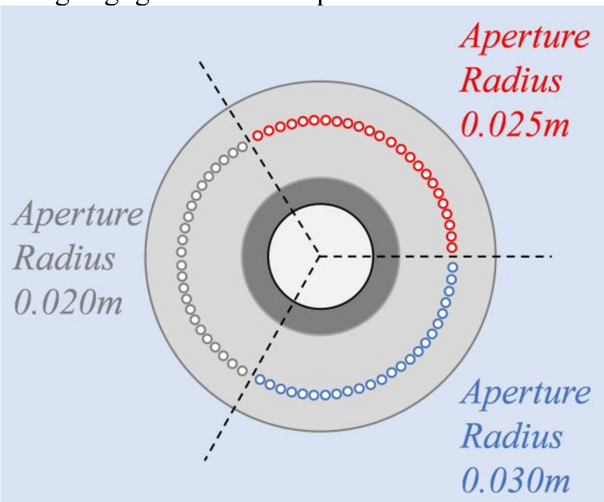

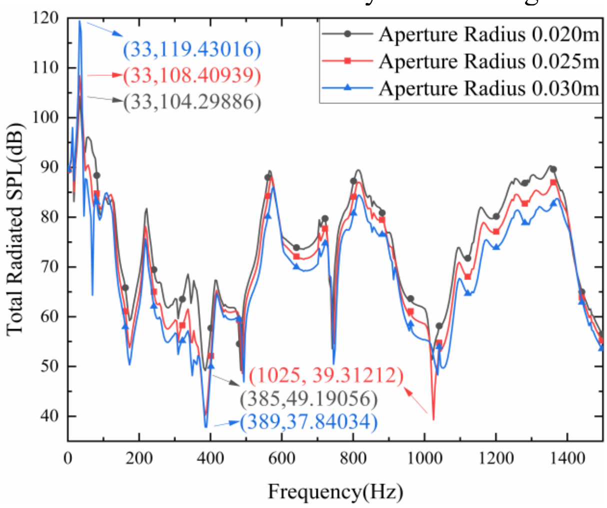

Figure 6. Acoustic overlay shell model with pore sizes. **Figure 7.** Radiated SPL comparison: Pore sizes.

4.3. Comparison of radiated SPL by various pore shapes configurations in acoustic metasurfaces
The cylindrical shell is equipped with circular pores of radius $0.025\ m$, triangular pores with heights equivalent to circular pores of diameter, and square pores circumscribed within the circular boundary, as depicted in Figure 8. Figure 9 demonstrates that the circular pore configurations yield the lowest radiated SPL across the entire frequency range, outperforming both triangular and square geometries [16].

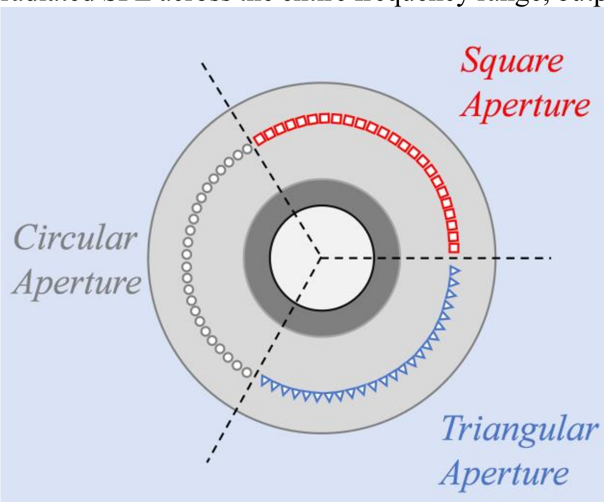

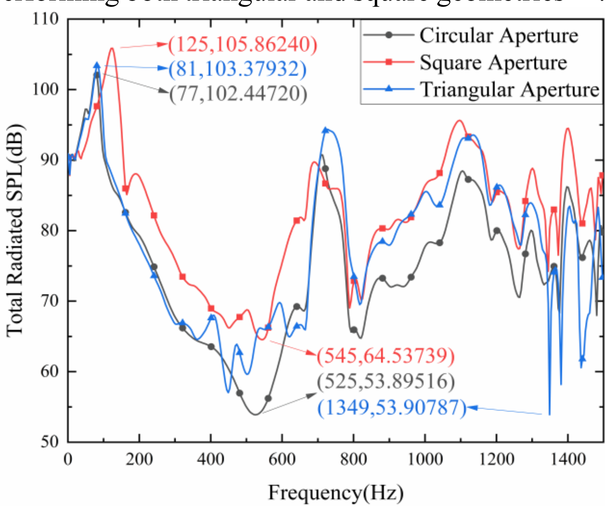

Figure 8. Acoustic overlay model with pore shapes. **Figure 9.** Radiated SPL comparison: Pore shapes.

4.4. Comparison of radiated SPL by various pore positions configurations in acoustic metasurfaces
Figure 10 delineates distributed pore configurations within viscoelastic coatings at the geometric centroid and radial ± 0.02 m offsets. Figure 11 quantitatively evaluates the frequency-dependent acoustic radiation parametric stimulations, revealing suppressed low-frequency SPL for peripherally positioned pores under invariant parametric constraints. The radiated acoustic pressure spectra for distinct pore positions exhibit negligible morphological divergence and nearly identical spectral evolution trends, whereas pores proximal to the outer periphery of viscoelastic coatings induce a spectral shift toward lower frequencies, thus enhancing the absorption efficiency over designs with centrally positioned pores.

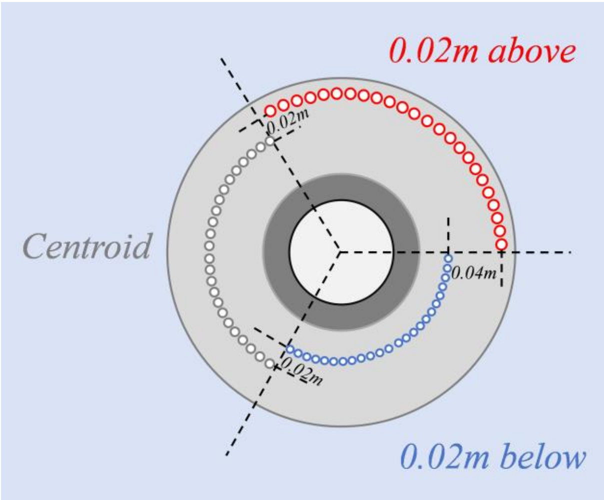

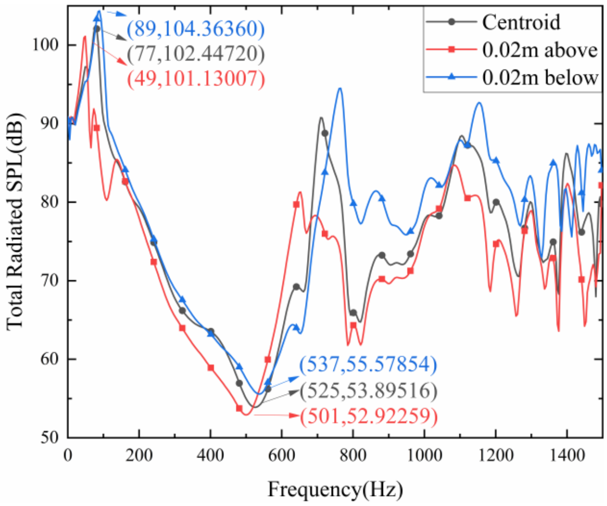

Figure 10. Acoustic overlay model with pore positions. **Figure 11.** Radiated SPL comparison: Pore positions.

4.5. Comparison of radiated SPL by various pore multi-row configurations in acoustic metasurfaces

The computational comparative analysis of radiated SPL is performed for cylindrical shells with multi-row acoustic metamaterial configurations, evaluating aligned circular pores of radius $0.015\ m$ radially arranged in one-, two-, and three-row longitudinal patterns on viscoelastic-coated cylindrical shells, with geometries schematically defined in Figure 12. Figure 13 quantifies the frequency-dependent acoustic radiation characteristics, revealing that multi-row pore arrays suppress SPL at lower frequencies under invariant parametric conditions. The radiated sound pressure spectra of multi-row pore configurations exhibit negligible morphological variation and nearly identical spectral evolution trends. In contrast, the single-row configuration shows substantially elevated SPL than multi-row configurations. At higher frequencies, multi-row configurations demonstrate minimal divergence in radiation performance.

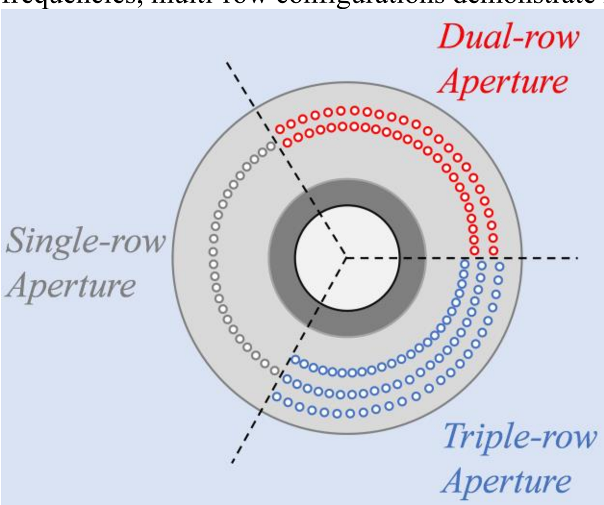

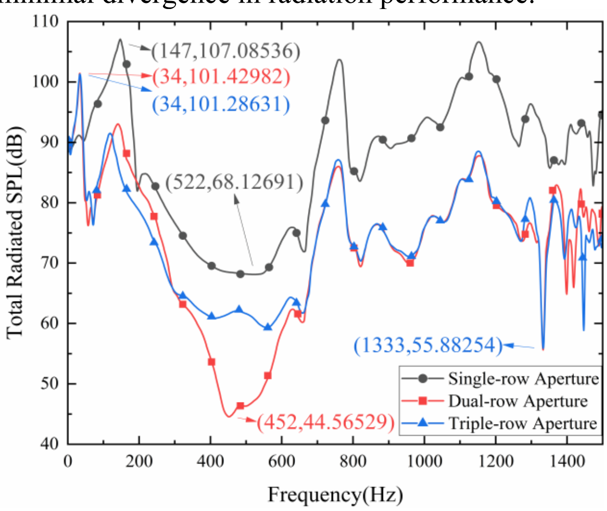

Figure 12. Acoustic overlay model with pore rows. **Figure 13.** Radiated SPL comparison: Pore rows.

5. Conclusion

This paper comprehensively elucidates vibroacoustic coupling mechanisms in a submerged cylindrical shell clad with multilayer viscoelastic coatings. It presents rigorous analytical derivations of effective acoustic impedance and interfacial continuity conditions governed by generalized admittance boundary constraints. The study also formulates radiation pressure through coupled acoustic–structure interactions, quantitatively compares the radiated sound pressure level (SPL) between engineered and pristine shells, and systematically analyzes the effects of pore-parameter dependencies—including morphological, dimensional, and spatial configurations—on broadband acoustic attenuation. Fundamental discoveries and core conclusions derived from the hybrid experimental-computational methodology are summarized:

1. The radiated SPL of a multilayer-coated cylindrical shell within the $100\sim500$ Hz frequency band exhibits a $50\ dB$ attenuation, due to optimized acoustic impedance matching and enhanced thermoviscous damping via the stratified coating design. The incorporation of pore-coated layers attenuates radiated SPL at frequencies beyond $100\ Hz$, demonstrating significant sound absorption capability.

2. The proximity of pores to acoustic-structure interfaces shifts the attenuation peak toward lower frequencies, enhancing significant resonance-based attenuation across the entire frequency spectrum.

3. Square apertures demonstrate a $5\ dB$ superior radiation suppression above $100\ Hz$ relative to both circular and triangular geometries, whereas triangular configurations exhibit a $5\ dB$ elevated SPL across the $700\sim800$ Hz band due to vortex shedding-induced pressure fluctuations at sharp aperture edges. Compared to shells featuring circular and triangular apertures, those with square apertures display a progressive reduction in acoustic radiation with increasing frequency, yielding the lowest total radiated sound pressure. On the contrary, shells with triangular configurations consistently produce higher SPL over the whole frequency range rather than square and circular configurations.

4. Single-row aperture configurations exhibit spectrally ascending SPL elevation of $10\ dB\sim15\ dB$ above $600\ Hz$, while multi-row aperture configurations realize acoustic emission stabilization with less than $1.5\ dB$ fluctuation via phase-cancellation mechanisms from coherently scattered wavefronts. The radiated SPL is consistently higher for single-row apertures, and the disparity becomes more pronounced with increasing frequency relative to shells with multi-row configurations, where radiated SPL stabilizes negligible divergence and convergence at similar levels at higher frequencies.

References

[1] Erwin Meyer and Ernst-Georg Neumann. Physical and Applied Acoustics: An Introduction [M]. New York, Academic Press, 1972.
[2] Ivansson, Sven M. Numerical design of Alberich anechoic coatings with superellipsoidal cavities of mixed sizes [J]. Journal of the Acoustical Society of America, 2008, 124(4): 1974-1984.
[3] Sharma G S, Skvortsov A, MacGillivray I, et al. Sound absorption by rubber coatings with periodic voids and hard inclusions [J]. Applied Acoustics, 2019, 143: 200-210.
[4] Leroy V, Strybulevych A, Lanoy M, et al. Super-Absorption of Acoustic Waves with Bubble Meta-Screens [J]. Physical Review B, 2015, 91(2): 020301.1-020301.5.
[5] Lee H, Jung M, Kim M, et al. Acoustically sticky topographic metasurfaces for underwater sound absorption [J]. The Journal of the Acoustical Society of America, 2018, 143(3): 1534.
[6] Hasheminejad S M and Safari N. Acoustic scattering from viscoelastically coated spheres and cylinders in viscous fluids [J]. Journal of Sound and Vibration, 2005, 280(1-2): 101-125.
[7] Pierre Méresse, Audoly C, Charles Croënne, et al. Acoustic coatings for maritime systems applications using resonant phenomena [J]. Comptes Rendus Mécanique, 2015, 343(12): 645-655.
[8] J X Hou, H C Zhu, S W Yuan, et al. Sound transmission characteristics of underwater flexible micro-perforated panels [J]. Applied Acoustics, 2021, 181.
[9] D Q Yang. Structural Dynamics of Ships and Offshore Units [M]. Shanghai, Shanghai Jiao Tong University Press, 2023.09.
[10] Y Y Zuo, D Q Yang, et al. Broadband transient vibro-acoustic prediction and control for the underwater vehicle power cabin with metamaterial components [J]. Ocean Engineering, 2024, 298.
[11] Sharma G S, Marsick A, Maxit L, et al. Acoustic radiation from a cylindrical shell with a voided soft elastic coating [J]. The Journal of the Acoustical Society of America, 2021, 150(6): 4308-4314.
[12] Sharifi M J, et al. Investigation of the underwater sound absorption and damping properties of polyurethane elastomer [J]. Journal of Thermal Analysis and Calorimetry, 2022, 147: 4113-4118.
[13] Y N Zhang and L Cheng. Ultra-thin and broadband low-frequency underwater acoustic meta-absorber [J]. International Journal of Mechanical Sciences, 2021, 210.
[14] D Q Yang, Q Li, X W Zhang, et al. Design Theories and Methods of Metamaterials in Ship Vibration and Acoustics [M]. Shanghai, Shanghai Jiao Tong University Press, 2023.06.
[15] Marsick A, Sharma G S, Eggler D, et al. On the vibro-acoustic response of a cylindrical shell submerged near a free sea surface [J]. Journal of Sound and Vibration, 2021, 511.
[16] L M Zhang and D Q Yang. Review on the applied research of mechanical and acoustic metamaterials in ship engineering [J]. Chinese Journal of Ship Research, 2023, 18(2): 1-19, 47.